Statistical, morphological, and corrosion behavior of PECVD derived cobalt oxide thin films

Azadeh Jafari[1] · Mohammad Hosein Alam[2] · Davoud Dastan[3] · Siamak Ziakhodadadian[4] · Zhicheng Shi[5] ·
Hamid Garmestani[3] · Alex S. Weidenbach[6] · Ştefan Ţălu[7]

Abstract

Experimental parameters have direct influences on materials properties and therefore their applications. The effect of plasma power on the properties of cobalt oxide thin films, prepared using plasma-enhanced chemical vapor deposition technique, on stainless steel substrates have been addressed in this paper. The structural, morphological, and compositional properties of these films were investigated by means of X-ray diffraction (XRD), atomic force microscopy (AFM), and X-ray photoelectron spectroscopy (XPS) technique. The XRD patterns demonstrated the growth of polycrystalline Co_3O_4 thin film with a cubic spinel structure such that the intensity of (511) and (311) peaks increase as the plasma power increases to 100 W. It is observed that crystallite size increases by increasing the plasma power and the maximum crystallite size is found to be 64.8 nm for 100 W. The AFM results illustrate that the surface roughness and grain size increase by increasing the plasma power, and the film deposited at lower plasma power has more uniform and smoother surface, mainly owing to the increase in surface diffusion that in turn causes the coalescence of the grains. The results of XPS spectra indicated the formation of Co_3O_4 thin films on stainless steel substrates and there were no other elements other than Co, O in the XPS spectra. Additionally, stereometric analysis and fractal dimension of the 3-D surface microtexture of the AFM micrographs were analyzed and the Kolmogorov–Smirnov test was used to assess the normal distribution of quantitative variables. The results of statistical analysis corroborated the experimental results and proved that the surface roughness increased upon an increase in plasma power. Moreover, the corrosion behavior and the surface morphology of the cobalt oxide thin films were investigated using the potentiodynamic method and scanning electron microscopy. The results of these analysis proved that as the plasma power increases the corrosion resistance improves against the H_2SO_4. The sample which deposited at 100 W plasma power has the minimum corrosion current and the corrosion resistance of steel substrate was improved by controlling the anodic reactions resulted from a protective Co_3O_4 thin film. These results are useful for building and designing stainless steel devices in corrosive environments.

✉ Zhicheng Shi
  zcshi@ouc.edu.cn

  Davoud Dastan
  davoud.dastan@mse.gatech.edu

[1] South Ural State University, 76, Lenin Aven, Chelyabinsk, Russia 454080

[2] Department of Electrical Engineering, Sharif University of Technology, Tehran, Iran

[3] School of Materials Science and Engineering, Georgia Institute of Technology, Atlanta, GA 30332, USA

[4] School of Chemistry and Chemical Engineering, Shanghai Jiao Tong University, Shanghai 200240, People's Republic of China

[5] School of Materials Science and Engineering, Ocean University of China, Qingdao 266100, People's Republic of China

[6] School of Electrical and Computer Engineering, Georgia Institute of Technology, Atlanta, GA 30332, USA

[7] Technical University of Cluj-Napoca, The Directorate of Research, Development and Innovation Management (DMCDI), Constantin Daicoviciu St., No. 15, 400020 Cluj-Napoca, Cluj County, Romania

1 Introduction

Semiconductor oxides have been vastly investigated due to their excellent physical, chemical, optical, and electrical properties [1–10]. Cobalt oxide is one of the most frequently used transition metal oxide in the last 2 decades, with direct and indirect band gap of 2.10 and 1.60 eV, respectively [11–13]. It can be used as a supercapacitor, gas sensor, solar selective absorber, fuel cells, catalysis, and lithium ion battery because of its anti-interference property, high surface area, and electrochemical stability [14–18]. It has generally two stable phases in the form of Co_3O_4 and CoO, with the normal spinel and the rock-salt structure, respectively. The advantages of Co_3O_4 over the CoO phase include its relatively high electrochromic efficiency (≈ 25 cm^2/C), large surface area, high conductivity, and better electrochemical stability. Various techniques have been used for the preparation of cobalt oxide, including spray pyrolysis, the thermal decomposition, sol–gel technique, chemical vapor deposition (CVD), and sputtering [14–22].

Maruyama et al. fabricated polycrystalline cobalt oxide thin films by a low-temperature atmospheric-pressure chemical vapor deposition method at a reaction temperature above 300 °C [17]. Donders et al. studied the properties of cobalt oxide thin films deposited using atomic layer deposition (ALD) and $CoCp_2$ (or cobaltocene is an organocobalt compound with the formula $Co(C_5H_5)_2$) as a cobalt precursor within a wide temperature window (100–400 °C) [18]. Similarly, Han et al., reported the deposition of cobalt oxide thin films at 68–138 °C using alternating injections of dicobalt hexacabonyl *tert*-butylacetylene (CCTBA) and ozone, they found that the films deposited at low temperatures showed excellent step coverage [20]. Maruyama et al. prepared cobalt oxide thin films using chemical vapor deposition and cobalt(II) acetylacetonate as the source material at a substrate temperature of 250 °C [21].

Jung et al. synthesized CoO_x thin films on thermally grown SiO_2 substrates by atomic layer deposition (ALD) using bis cobalt ($C_{16}H_{32}N_4Co$). This study revealed that pure Co_3O_4 phase could be grown at a relatively low temperature (250 °C) using water vapor as a reactant [23]. The coating process accelerates while using plasma in the PECVD technique and the thermal shock reduces on the substrate. The uniform coating of different shapes is possible when the plasma operates at low temperatures. An important advantage of PECVD deposition is that the deposition temperature is usually quite low, which works great for materials which are temperature sensitive or that get their characteristics changed at high temperatures. The other benefits of PECVD include: good step coverage, highly uniform film deposition, excellent control of material properties (refractive index, stress, hardness, etc.) [24].

Recent research applies this technique to deposit nano-structured films: By plasma-enhanced chemical vapor deposition, a molybdenum disulfide (MoS_2) thin film is synthesized directly on a wafer-scale plastic substrate at below 300 °C [25]. Also, microcrystalline hydrogenated-silicon (μc-Si:H) films has been deposited in a plasma-enhanced chemical vapor deposition in the temperature range between 70 and 250 °C [26]. Titanium oxide thin films were prepared on p-Si(l00) substrate by plasma-enhanced chemical vapor deposition using high purity titanium isopropoxide and oxygen [27]. High-quality ZnO thin films deposited at low temperature (200 °C) by pulsed plasma-enhanced chemical vapor deposition (pulsed PECVD) [28]. Stainless steels are extensively used in industrial fields due to their high corrosion resistance, good mechanical properties and cheapness comparing to other metals [29].

On the other hand, stainless steel has the tendency to corrode in an aggressive environment; therefore, it is important to further improve its corrosion resistance in these mediums. In this study, we investigated the corrosion behavior of cobalt oxide thin films deposited on steel stainless substrates using PECVD technique for the first time. Moreover, the crystal structure and the morphology of Co_3O_4 thin films were studied for various plasma power by means of XRD, AFM, and SEM. Also, the XPS and the corrosion tests have been used to study the compositions and of corrosion properties of the samples. To the best of our knowledge, the plasma power dependent variation of structural, morphological, and corrosion property of cobalt oxide thin film has not been reported previously by PECVD.

2 Experimental method

2.1 Materials and film preparation

The homemade PECVD cluster tool system, used in this study, was described before [30]. The DC-PECVD apparatus used in our experiments is composed of a Pyrex chamber, a gas mixer, vacuum pumps and gas cylinders. A schematic of the PECVD set-up is shown in Fig. 1. The central part of the DC-PECVD is a cylindrical process chamber with a diameter of 28 cm consisting of a base and a cover. After the chamber is pre-evacuated by rotary pump, the base pressure of the system is reached to $\approx 10^{-2}$ Torr. The substrate is placed on a furnace right under the anode. The temperature of the substrates is monitored by a thermocouple. The distance between the two electrodes is 1.5 cm. The 316L stainless steel (S.S.316L) is used as a substrate and cut into 1×1 cm^2 pieces. They were clean using acetone, alcohol and deionized water. Subsequently, the substrate is heated up to the desired temperature (350 °C) and a mixture of Ar/O_2 in the ratio 85:15 introduces into the chamber. In our

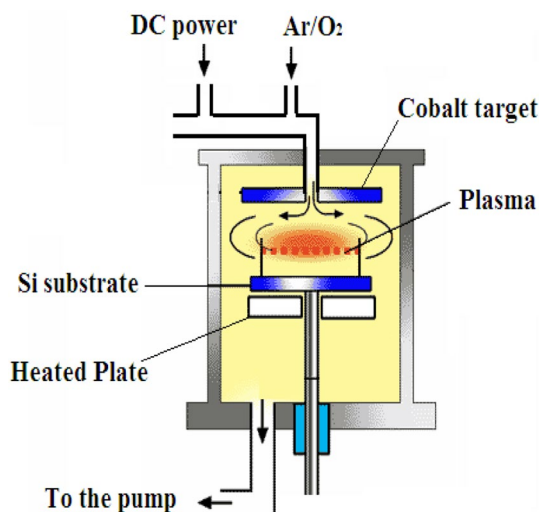**Fig. 1** Schematic of the PECVD set-up

Fig. 2 X-ray diffraction patterns of Co_3O_4 films at different plasma power: (a) 80 W (b) 90 W, and (c) 100 W

experiments, the oxygen level and the substrate temperatures were equal and the total gas pressure was kept fixed at 10^{-2} Torr by adjusting the gas outlet valve.

The plasma power was varied from 80 to 100 W. After a deposition time of around 15 min, the sample was rapidly cooled to the room temperature at a cooling rate of about $10 \, °C \, s^{-1}$ by turning off the heater. During the cooling process, the ionized non inert gas can react chemically with the cobalt target material and produce a molecular compound and then deposit the films. In fact, with Ar/O_2 bombardment on cobalt target and reaction of cobalt with oxygen in plasma, the cobalt oxide is deposited. The plasma is created by DC discharge between the substrate and the cobalt target, and the space between them is filled with the oxygen and argon. Finally, the temperature of the plasma reaches at a sufficiently high level in order to ionize the filling gas species completely. In the current experiments, the ions of oxygen and argon are formed and accelerated earlier than the cobalt ions because they have substantially higher energy levels.

2.2 Characterization techniques

The structure properties of the cobalt oxide thin films were characterized by X-ray diffraction (XRD) analysis using the STOE model STADI MP system and Cu kα radiation with a tungsten filament at 40 kV, 40 mA and step size of 0.04. AFM technique was used to study surface topography and roughness (SPM Auto Probe CP, Park Scientific Instruments, USA). X-ray photoelectron spectroscopy technique (Thermo Scientific, K-Alpha) was used to study the elemental composition of Co_3O_4 thin films. The surface morphology of cobalt oxide thin films was investigated using the scanning electron microscope (SEM, LEO440i) after the corrosion test. The
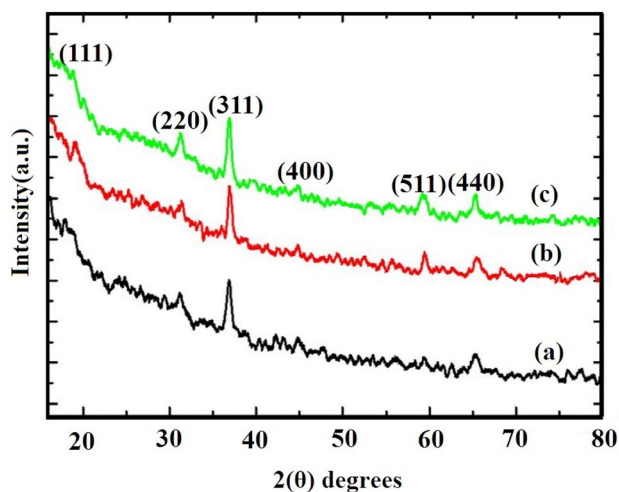
electrochemical corrosion of the Co_3O_4 surfaces was studied by means of potentiodynamic method (potentiostat model EG&G, Princeton 273A).

3 Results and discussion

3.1 XRD analysis

Figure 2 demonstrates the XRD patterns of all cobalt oxide thin film on S.S.316L substrates prepared using the PECVD method at different plasma powers. The XRD spectra show that all the films are polycrystalline with a cubic spinel structure and a random orientation, which generally occurs in the growth of Co_3O_4 thin films. Cobalt oxide is an antiferromagnetic material with mixed valence (Co^{3+} and Co^{2+} ion) and regular spinel structure having Co^{3+} in octahedral sites and Co^{2+} in tetrahedral sites [20, 21]. All the peaks in the XRD patterns are correspond to (111), (220), (311), (400), (511), and (440) planes which are well matched with the standard JCPDS data. Polycrystalline films deposited on substrates generally show preferred orientation, with a strength which depends on the preparation method, materials, and deposition conditions including the source power.

It is clear from Fig. 2 that the intensity of the peaks especially (511) and (311) peaks increase as the plasma power increases to 100 W. Variations in measured intensity are related chiefly to variations in the scattering intensity of the components of the crystal structure and their arrangement in the lattice. High intensity or sharp peak is an indication of more order, crystallization, and arrangement. Preferred orientation results in some Bragg planes to be more exposed to X-rays. The peak (511) is due to X-ray

diffraction from the (511) planes. The preferred orientation of a film is due to its lowest overall energy, which is a result of competition between the surface energy, the strain energy, and the stopping energy of different lattice planes, here the (511) and (311) planes has the lowest strain energy and strain energy have affected the film growth process [28] which can be impressed by plasma power. An increase in power increases the intensity of the diffraction peaks indicating the increase in crystallinity of the films.

This could be due to the fact that at low plasma power, the reaction between oxygen atoms/molecules and cobalt is not favored even though reactive gas species as radicals can be generated at high density and relatively low temperature with the assistance of plasma. The gas mixture ratio, gas flow, plasma power, and pressure can influence the densities of ions and radicals and when a high power plasma is used, the ion density can be high enough to sputter a significant amount of the cobalt target [28, 30]. Radicals are chemically unsaturated and therefore capable of chemical reaction at high rates, they are species that react at a surface and contribute from film formation. One can picture the PECVD process as a sequence of three distinct processes: the chemical activation of gas molecule through electron impact dissociation, the transport of the radical species to the substrate and the chemical reaction at the film. Gas flow velocities are so low that neutral radicals created in the plasma find their way to the surface of the film by diffusion. The concentration gradient driving the diffusion process is maintained by the radical generation in the plasma (10^{14} cm^{-1}) and their disappearance at the film surface (0 cm^{-1}) [31].

Radical formation is suppressed with increasing gas flow rate and temperature, and is enhanced with increasing power. Low power and process pressure reduce the density of radical gas and a short inter-electrode distance reduces the distance over which the radical must travel before it bonds to the film surface [32]. However, it has been shown that dust particles tend to generate during the film deposition that leads to the degradation of the film surface morphology. Dust particles generated in the plasma become negatively charged due to the higher mobility of electrons over ions and consequently undergo levitation by the large electric field in the sheath region. Particles are in many cases trapped at a certain region of plasma [32]. The size of dust particle and the structure of particle clouds trapped are strongly depend on the plasma operating condition and these also in turn influence the level of particulate contamination of the substrate. It has been shown that dust particles may deposit into the growing films during the continuous plasma operation, not at the end of the film preparation when the plasma is turned off. Dust particles can escape the plasma and cause the degradation of film properties. Moreover, while unloading samples and after the disposition or during analysis,

there is a chance to have impurities on the surface of the films [31, 33].

While forming Co_3O_4 film on the S.S.316L substrate, ionized oxygen and argon atoms are accelerated towards the cobalt target surface, thus, all surfaces exposed to the plasma receive energetic ion bombardment which can help remove contaminants. As the plasma power increased from 80 to 100 W, the surface ad-atom mobility increases and electrons move faster towards the substrate. The vapor atoms are continuously depositing on the surface. Depending on the atom's energy and the position at which it hits the surface, the impinging atom could re-evaporate from the surface or adsorb to it, becoming an ad-atom. In growth process of thin film, diffusion and mobility of ad-atoms on the surface is important, which is controlled by substrate temperature, substrate bias during deposition, and pressure. Beside of thermodynamic consideration, kinetic mechanism of ad-atom attachment for the stable nuclei formation or growth of stable cluster has to be taken into account. Ad-atom must have the surface mobility enough for the island formation in the film growth process. The higher mobility of ad-atom at higher temperature are well coordinated with the result that crystalline nuclei density is decreased as temperature is increased [31–33].

The absence of a cobalt peak in the XRD pattern indicates that a complete oxidation occurred owing to the high value of mixture of Ar/O_2 gas flow rate during the deposition process (10 sccm). Here, we use the well-known Scherrer's formula to calculate the crystalline size, which is widely used to calculate grain size of materials. The average crystallite size in Co_3O_4 thin film is calculated using the full width at half-maximum (FWHM) of (311) peak from the following Scherrer's formula [16, 34–39] and the results are presented in Table 1.

$$D = k\lambda/\beta\cos\theta \tag{1}$$

where, k is the shape factor (0.94), λ is the wavelength of Cu Kα radiation (1.5406 Å) and β is the full width at the half-maximum. It is observed that crystallite size increases by increasing the plasma power during the growth process. The maximum crystallite size is found to be 64.8 nm for 100 W. The results show that the crystallite size gradually increases

Table 1 Effect of plasma power on Co_3O_4 thin film structure

Sample number	Plasma power (W)	Crystallite size (nm) ± 0.5 from XRD	Roughness rms (Å) from AFM	Grain size (nm) from AFM	Corrosion current density (µA/cm^2)
A	80	52.3	17	84.5	0.007
B	90	58.2	52	98.4	0.010
C	100	64.8	91	107.1	0.002

with increasing plasma power due to energetic ion bombardment. Therefore, when the plasma power increases further, the ion density becomes large enough for crystal growth. Our results are in agreement with the reported results by other researchers. El-Hossary et al. investigated the effect of plasma-processing power on structural of Ti–Zr–N thin film using DC-pulsed magnetron sputtering method. The results demonstrated that the grain size increased as the plasma-processing power increases [40]. Vopsaroiu et al., studied variation of the mean grain size with sputtering conditions such as plasma power, bias voltage, and process pressure. The results showed that the mean grain diameter increases upon increasing the plasma power [41].

3.2 AFM analysis

Atomic force microscopy (AFM) is a convenient technique to study the morphology and roughness of thin films. Figure 3a–c depicts three-dimensional (3D) AFM images of the cobalt oxide thin films for 80, 90, and 100 W plasma power, respectively. The summary of surface roughness parameters are given in Table 1. Grain sizes of all samples were measured from 2D AFM images using JMicrovision Code. These surfaces have a characteristic fractal auto-affine symmetry, with a cauliflower morphology where smaller grains aggregate to form larger grains. Another noticeable observation in Fig. 3 is that the grain size and surface roughness increased by increasing plasma power. The grain may consist of more than one crystallite that its size is measured by XRD. AFM gives the grain size that measured by the distances between the grain boundaries and for this reason, the measured grain size by AFM is different from that measured by XRD as noticed from Table 1. The AFM 3D images show that the substrates are covered with grains of different sizes and reveal that the film deposited at lower plasma power has more uniform and smoother surface whose values of root mean square roughness (RMS) confirm this behavior (Table 1). In fact, as a result of increasing the bombardment of the cobalt surface by more numerous species present at high power plasma, more radicals are produced and therefore, increasing the plasma power increases the surface roughness [33, 35].

According to the previous studies [30, 33], the structure and morphology of PECVD-grown nanostructured materials is strongly determined by substrate-plasma species interaction. Surface roughness analysis of SiO_2 thin layers for PECVD on different substrates was studied by Amirzada et al. They observed that the nature of the substrate does not remarkably influence the surface roughness of the grown layers [42]. It is also perceived that the value of the surface roughness increased as the deposition temperature of the PECVD process increased. In the other worked by Braz et al., a-C:H films were synthesized by PECVD under various deposition parameters and the results indicated that DLC phases showed different surface morphologies due to variations in the deposition parameters [43].

The amount and nature of plasma species depends on the plasma power, the position of the substrate in the plasma plume and gas composition ratio. Ions, electrons and neutral species play a key role during the nucleation and growth stages and the momentum, temperature and density of this species increase by increasing plasma power which effects on reaction kinetics and growth dynamics. The growth processes consist of the deposition of particles and the surface diffusion of ad-atoms. The stochastic nature of the deposition flux inherently generates a non-conservative noise which drives the crystal to grow. The surface diffusion of ad-atoms also generates a conservative noise which leads to smoothening of the surface. In Atomistic Edwards–Wilkinson Model [44] for thin film growth, particles fall randomly on the surface, then diffuse to the neighboring site with the greatest depth. In the Edwards–Wilkinson Model the surface looks basically flat from the distance, it develops deep valleys with high steps perpendicular to the substrate. The growth proceeds in a strip of infinite length and finite width, with periodic boundary conditions. In every time step a particle is added on top of a column of occupied sites with a randomly chosen substrate coordinate x. Then it looks around among the surface sites at the nearest neighbor which one offers the
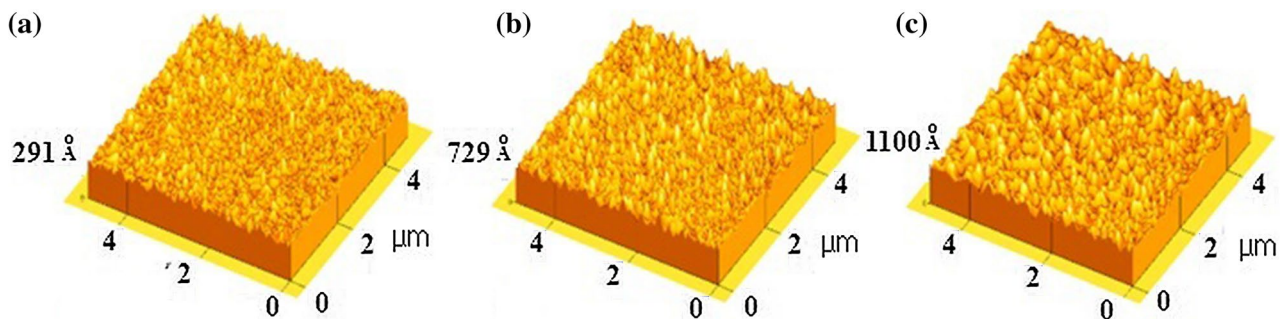

Fig. 3 The AFM images from the experimental results of the samples grown at various plasma power: **a** 80 W, **b** 90 W, and **c** 100 W

strongest binding, i.e., the most occupied neighbors. The particle moves to this site and sticks there. This is intended to simulate surface diffusion at not too high temperatures where the particles move only a short distance to find a favorable growth site before other particles are deposited on top of them. If there are as many bonds at x as next to x, the particle stays at x. If two sites next to x are equally preferable, one of them is chosen at random [45, 46]. The increase of the surface roughness of cobalt oxide thin film is due to the increased surface diffusion which in turn produces larger and deeper valleys between newly formed

grains; hence, larger grains and higher surface roughness are obtained for the films deposited at 100 W.

3.3 Statistical analysis

AFM images were selected for the statistical analysis. A series of five test samples of each group were analyzed and compared based on their 3-D surface texture characteristics (Figs. 4, 5 and 6). The 3-D surface characteristics of samples were quantified by measuring three locations on regions of each sample. Stereometric analysis of the 3-D
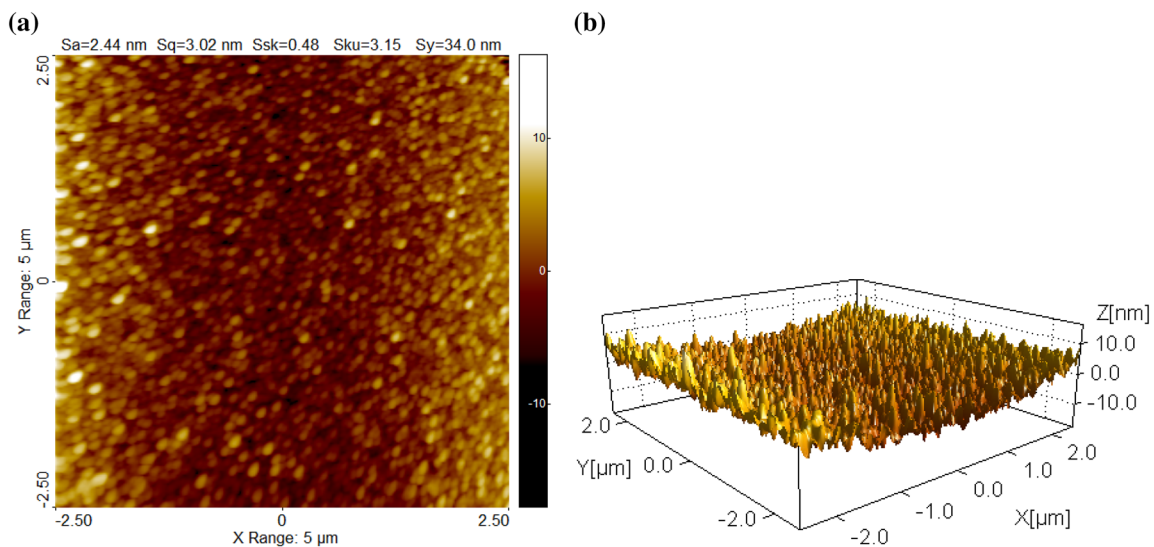

Fig. 4 The representative 2-D and 3-D topographic AFM images of statistical results of sample A in: **a** 2-D; **b** 3-D, scanning square areas of 5 µm×5 µm. The vertical range of the displayed data (in nanometers [nm])

Fig. 5 The representative 2-D and 3-D topographic AFM images of statistical results of sample B in: **a** 2-D; **b** 3-D, scanning square areas of 5 µm×5 µm. The vertical range of the displayed data (in nanometers [nm])
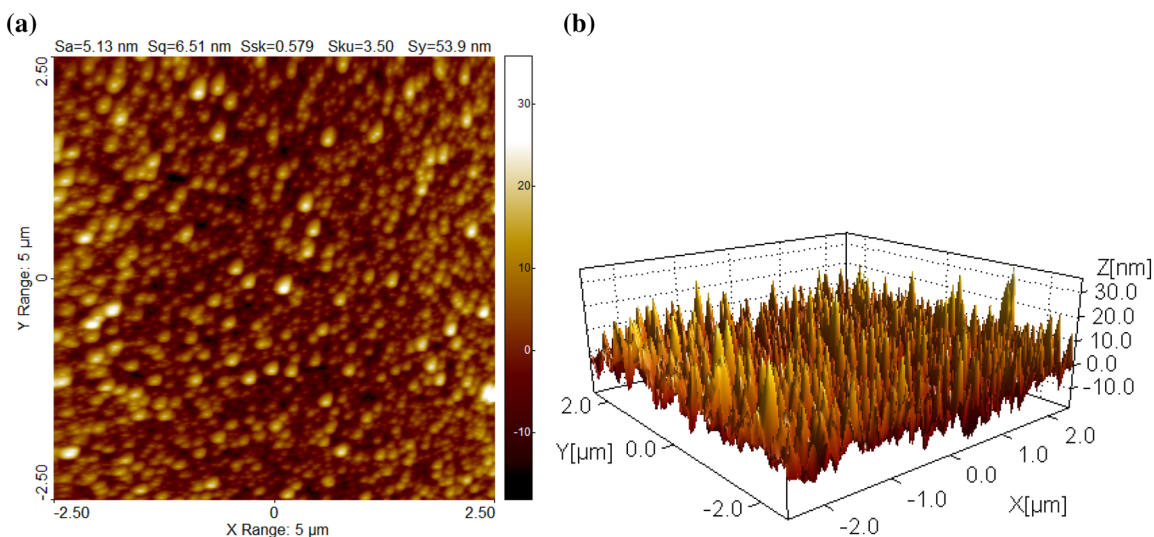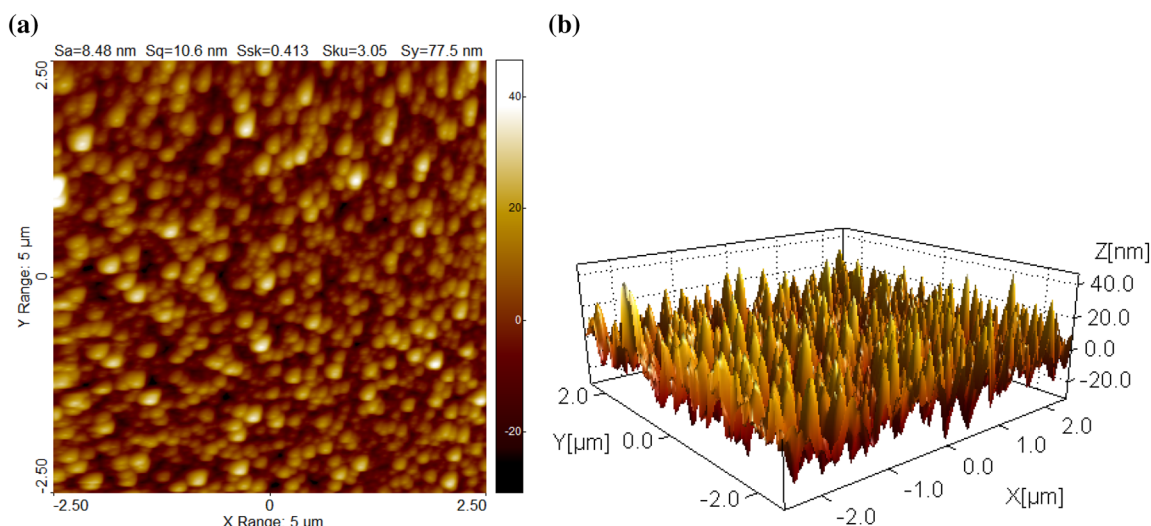
(a)

(b)

Fig. 6 The representative 2-D and 3-D topographic AFM images of statistical results of sample C in: **a** 2-D; **b** 3-D, scanning square areas of 5 μm×5 μm. The vertical range of the displayed data (in nanometers [nm])

surface microtexture of the AFM micrographs were analyzed with SPIP^{TM} 6.7.7 software [47] according to ISO 25178-2:2012 [48] and ASME B46.1-2009 [49, 50]. Statistical analyses were performed using the GraphPad InStat version 5.0 computer software package (GraphPad, San Diego, CA, USA). The Kolmogorov–Smirnov test was used to assess the normal distribution of quantitative variables. Comparisons among different areas within the same sample were performed using independent samples T test. When statistical significance was found, the difference between two groups was further compared using the Mann–Whitney U test. Differences with a P value of 0.05 or less were considered statistically significant. The average results were expressed as mean value and standard deviation.

The representative 3-D topographic AFM images of samples (A, B, and C correspond to Fig. 3a–c respectively), for scanning square area of 5×5 μm^2, are demonstrated in Figs. 4, 5, and 6, both in 2-D and 3-D. They are shown in 2-D and 3-D mode (in perspective view), with the vertical (height) scale [in nanometers (nm)] displayed in coding colors, according to the palette described by the respective side-bar on the right hand side of the AFM image. The fractal dimension, D is calculated for the different angles by analyzing the Fourier amplitude spectrum; for different angles the amplitude Fourier profile is extracted and the logarithm of the frequency and amplitude coordinates calculated. The fractal dimension, D, for each direction is then calculated as $D = (6 + s)/2$, where 's' is the (negative) slope of the log curves. The reported fractal dimension is the average for all directions [47]. The surface of group C has the most regular topography ($D_f = 2.23 \pm 0.02$, value lower than all the other sample values) and the most irregular surface ($S_q = 10.6 \pm 0.179$ nm); while the most irregular topography

($D = 2.37 \pm 0.04$, value bigger than all the other sample values) with the most regular surface ($S_q = 3.02 \pm 0.124$ nm) was found in group A (Table 2).

As can be seen from Table 3 Root mean square height increases by increasing plasma power. A possible reason for an increase in the surface roughness is the initial cluster size, which is formed at the beginning of deposition on the substrate. The PECVD deposition can be considered as an island or Volmer Weber growth process [51] in which the cluster size increases with the increase in substrate temperature [52], which causes increase in surface roughness. This is due to the coalescence mechanism, in which two clusters collide with each other and form a one big cluster, when they are in a random motion which is proportional to the substrate [53, 54].

3.4 XPS analysis

The XPS survey of the all samples have been plotted and showed in Fig. 7. There are no other elements other than Co, O in the spectra. Figure 8a, b depicts the X-ray photoelectron spectroscopy (XPS) of Co_3O_4 thin films. As can be seen, the XPS spectra of all three samples consist of Co and O

Table 2 The fractal dimension, Df, of the samples: A, B, and C. The average results were expressed as mean value and standard deviation

The parameter	Symbol	A Values	B Values	C Values	P [-] * Value
The fractal dimension	Df [-]	2.37±0.04	2.31±0.03	2.23±0.02	0.014

*Statistically significant difference: $P < 0.05$

Table 3 The statistical parameters of the samples: A, B, and C, according with ISO 25178-2: 2012 and ASME B46.1-2009

The statistical parameters	Symbol	A Values	B Values	C Values	P values * [-]
Amplitude parameters					
Arithmetic mean height	Sa (nm)	2.44 ± 0.119	5.13 ± 0.142	8.48 ± 0.162	0.012
Root mean square height	Sq (nm)	3.02 ± 0.124	6.51 ± 0.156	10.6 ± 0.179	0.015
Surface skewness	Ssk (–)	0.48 ± 0.02	0.579 ± 0.03	0.413 ± 0.01	0.011
Surface kurtosis	Sku (–)	3.15 ± 0.14	3.50 ± 0.18	3.05 ± 0.11	0.019
Maximum height	Sz (nm)	34.0 ± 1.99	53.9 ± 2.25	77.5 ± 2.97	0.021
Ten point height	S10z (nm)	19.45 ± 1.21	47.76 ± 1.74	71.82 ± 2.12	0.017
Maximum valley depth	Sv (nm)	17.77 ± 1.19	18.21 ± 1.22	31.06 ± 1.47	0.021
Maximum peak height	Sp (nm)	16.18 ± 1.17	35.71 ± 1.52	46.42 ± 1.62	0.024
Hybrid parameters					
Mean summit curvature	Ssc (1/nm)	0.0021	0.0131	0.0120	0.016
Area root mean square slope	Sdq6	0.079 ± 0.004	0.193 ± 0.008	0.257 ± 0.011	0.010
Surface area ratio	Sdr (%)	0.330 ± 0.011	1.907 ± 0.008	3.259 ± 0.114	0.025
Projected area	S2A (nm^2)	2.5E+07	2.5E+07	2.5E+07	–
Surface area	S3A (nm^2)	2.5E+07	2.5E+07	2.5E+07	–
Functional parameters					
Surface bearing index	Sbi	0.279 ± 0.008	0.272 ± 0.007	0.381 ± 0.010	0.022
Core fluid retention index	Sci	1.748 ± 0.032	1.788 ± 0.037	1.739 ± 0.029	0.026
Valley fluid retention index	Svi	0.085 ± 0.005	0.084 ± 0.004	0.087 ± 0.006	0.022
Reduced summit height	Spk (nm)	3.917 ± 0.142	9.607 ± 0.198	12.98 ± 0.237	0.012
Core roughness depth	Sk (nm)	7.836 ± 0.312	15.87 ± 0.512	27.25 ± 0.742	0.015
Reduced valley depth	Svk (nm)	1.923 ± 0.026	3.882 ± 0.029	6.38 ± 0.034	0.021
Spatial parameters					
Texture direction index	Stdi (–)	0.419 ± 0.022	0.797 ± 0.034	0.750 ± 0.031	0.017
Dominant radial wavelength	Srw (nm)	5000	5000	709.9	0.016
Radial wave index	Srwi (–)	0.030 ± 0.007	0.067 ± 0.014	0.166 ± 0.023	0.020
Mean half wavelength	Shw (nm)	416.7 ± 21	333.3 ± 15	384.6 ± 18	0.027
Correlation length at 20%	Scl20 (nm)	862.7 ± 15	98.04 ± 11	117.6 ± 12	0.024
Correlation length at 37%	Scl37 (nm)	529.4 ± 22	78.43 ± 16	98.04 ± 18	0.028
Texture-aspect ratio at 20%	Str20 (–)	0.01 ± 0.005	0.625 ± 0.037	0.75 ± 0.039	0.014
Texture-aspect ratio at 37%	Str37 (–)	0.01 ± 0.005	0.80 ± 0.034	0.83 ± 0.038	0.012
Cross hatch angle	Sch (°)	2.5 ± 0.92	10.76 ± 3.15	42.95 ± 5.51	0.021

The average results were expressed as mean value and standard deviation

*Statistically significant difference for all values: $P < 0$

elements, while there is no evident of impurities detected in any sample. Figure 8a exhibits the Co2p core spectrum of the cobalt oxide thin films at various plasma power, with a spin-energy separation of 15 eV, around 780 eV (2p3/2) and 795 eV (2p1/2), which is characteristic of a Co_3O_4 [55]. The core level centered at 531 eV (Fig. 8b) corresponds to the oxygen species in the Co_3O_4 phase. Additionally, no significant difference is observed in the position and intensity of XPS spectra for all cobalt oxide samples and the change in plasma power does not affect chemical bonding, elemental composition or chemical state of the elements in thin films.

XPS spectra of several compounds with well-defined surfaces are given as reference in Co 2p photoemission characterization. Preparation and characterization of these surfaces have been reported previously [56, 57]. The more complex structure in the CoO photoemission is a direct result of the nature of the valence band produced by octahedrally coordinated and high-spin Co^{2+} oxides. The high-spin character allows for strong electron correlation resulting in a range of closely lying states with vary d–d coupling, and the overlap of cobalt valence orbitals with surrounding O 2p allows for charge-transfer from O 2p to the Co 3d leading to the possibility of different final states in the photoemission mechanism [52]. These effects are not present in either low spin, octahedrally coordinated Co^{3+} or tetrahedrally coordinated Co^{2+} [57].
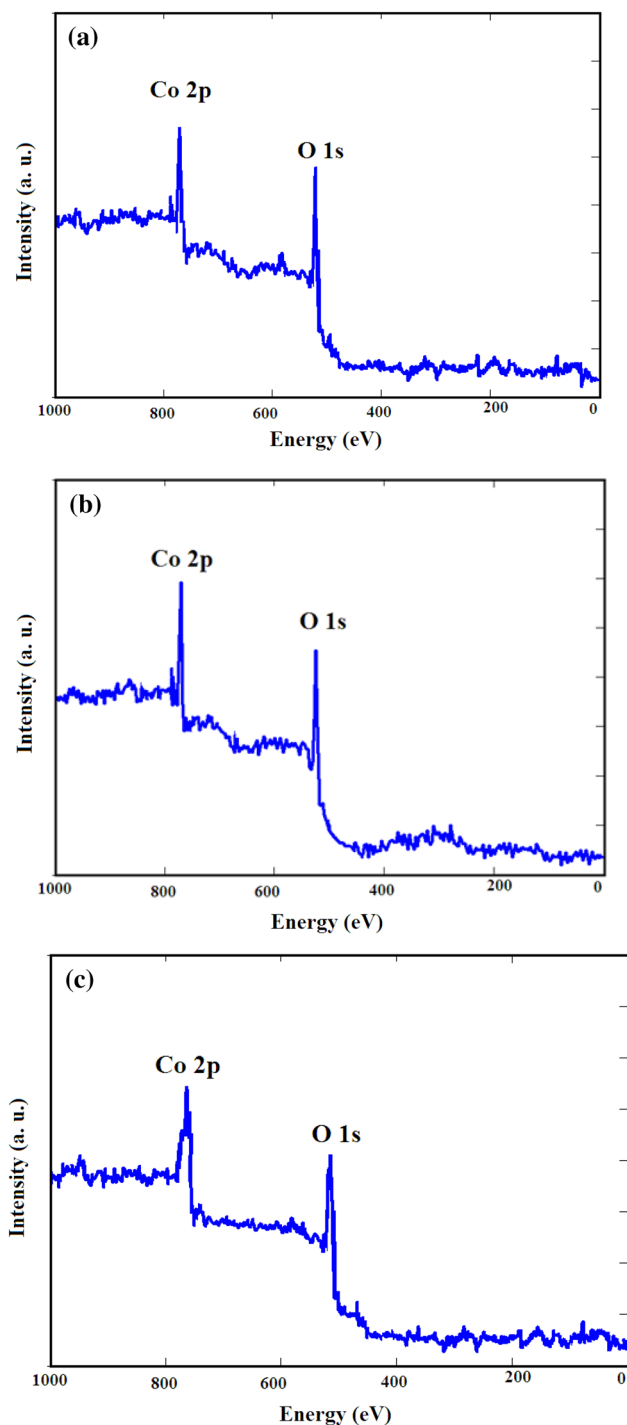
Fig. 7 XPS survey spectra of the samples grown at various plasma power: **a** 80 W, **b** 90 W, and **c** 100 W

3.5 Corrosion property

Figure 9a–d shows potentiodynamic curves of cobalt oxide thin films at different plasma powers.

Figure 9a is the polarization spectra of stainless steel substrate and Fig. 9c, d are the potentiodynamic graphs of

cobalt oxide thin films grown on stainless steel substrates at 80, 90, and 100 W plasma power. The potential which was measured by saturated calomel electrode (SCE) as a reference electrode was scanned from -700 mV to approximately $+1500$ mV versus open circuit potential (OCP) at the scan rate of 1 mV/s. To investigate the effects of the Co_3O_4 thin film coating on corrosion properties of stainless steel substrates, the test of stainless steel substrate was carried out at the same time (Fig. 9a). The corrosion current density values obtained from the Tofel slope technique are given in Table 1.

As can be seen in Fig. 8a–d, the propensity to corrosion decreases and the corrosion protection of samples remarkably improves by deposition of Co_3O_4 thin films on stainless steel (Table 1). The sample which deposited at 100 W plasma power (Fig. 8d) has the minimum corrosion current, and the maximum corrosion current is related to the sample prepared at 80 W plasma power (Fig. 9b). The corrosion current density values are very small and anodic branch of polarization curves has fluctuations, therefore, we conclude that both of steel substrate and Co_3O_4 thin film on steel substrate samples are located in the passive region in a corrosion solution containing 0.5 M H_2SO_4. The corrosion resistance of steel substrate was improved by controlling the anodic reactions resulted from a protective Co_3O_4 thin film for the corrosion current density of 0.03 µA/cm^2 [58–60].

Figure 10a–d illustrates SEM images of stainless steel substrate and Co_3O_4 thin film grown on stainless steel substrates at various plasma power after the corrosion test. From the comparison between SEM image of the pristine stainless steel substrate (Fig. 10a) and those coated with Co_3O_4 thin films at 80, 90, and 100 W plasma power (Figs. 10b–d), we clearly observe that the Co_3O_4 thin film samples have remained more intact than the bare stainless steel and have less surface damages such as holes, pits, and cracks. This may be qualitatively achieved by the extent of damage occurred on these samples after corrosion test. In addition to that, it can be observed that the SEM image of the sample deposited at 100 W (Fig. 10d) shows the least amount of corrosion attack on its surface and therefore, the samples coated with Co_3O_4 thin film show an obvious promotion in electrochemical corrosion resistance.

Other research work on an nanocrystalline coating agreed that the nanocrystalline structure gave better corrosion resistance than the microcrystalline one, since a higher grain boundary density in the nanocrystalline structure speeded up the formation of a stable and protective oxide layer [61, 62]. This indicates that finer grain sizes of the coating might provide defect sites at the grain boundaries which makes the corrosion easier to initiate at these active sites [63]. Morral demonstrated that the corrosion resistance of cobalt-base industrial alloys films depends on metal and alloy composition, pressure, temperature, and
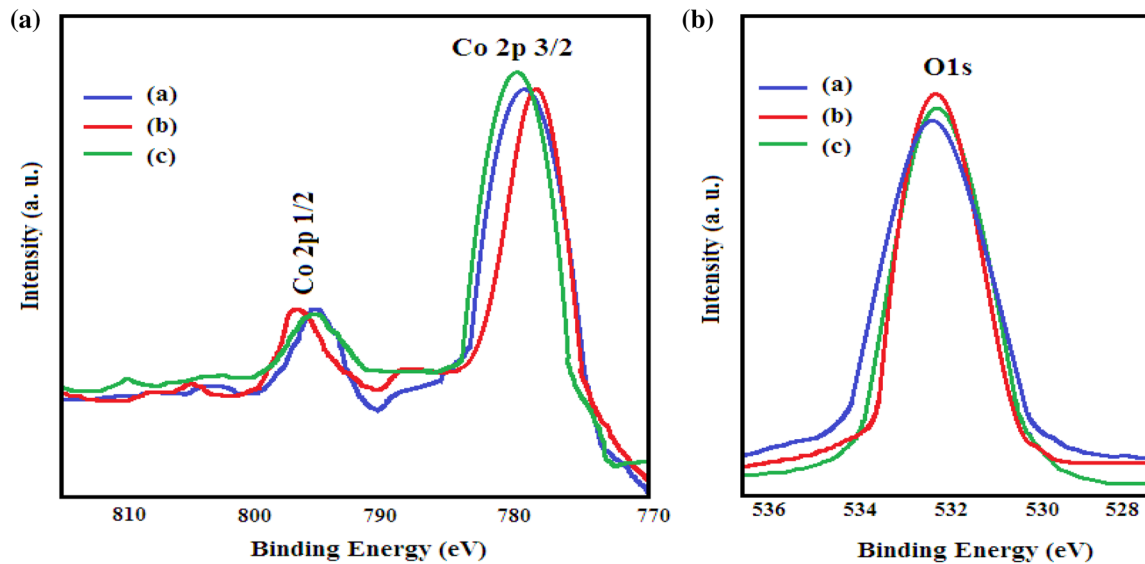
Fig. 8 **a** Co2p and **b** O1s XPS spectrum of the samples grown at various plasma power: (a) 80 W, (b) 90 W and (c) 100 W

time. Additional factors, alone or in combination, such as surface preparation, stress, thermal shock, geometry of the part, velocity, density, and flow pattern of the corroding environment also have an effect. Also, it has been shown that the effect of impurities in metals and alloys may be as significant as that of added alloying elements; impurities may alter the scales' chemical and physical properties-increasing, decreasing, or neutralizing corrosion rates [64]. Moreover, Brandolt et al. obtained that the corrosion resistance of nickel and cobalt coatings by high-velocity oxy-fuel thermal spraying on steel. From the results of the polarization, both the nickel coating removed from substrate as well as the cobalt coating removed from substrate showed worse corrosion behavior compared with the respective pure metals. This confirms that the coatings obtained by thermal spraying feature a loss in corrosion performance [65].

4 Conclusions

Plasma-enhanced chemical vapor deposition technique was employed to deposit cobalt oxide thin films on steel stainless substrate. The influence of the plasma power was investigated on the physical properties of Co_3O_4 thin films. The results demonstrated the phase formation and increased surface roughness and grain size upon increase in the plasma power and the highest roughness and grain size were achieved for a plasma power of 100 W. Additionally, the results of corrosion study illustrated an enhancement in the corrosion resistance as the plasma power increases. Moreover, the corrosion resistance of steel substrate is enhanced by protective cobalt oxide thin film's layer that is useful for the designing and building novel devices and instruments. Furthermore, the results of statistical analysis and fractal dimension of the 3-D surface microtexture of the AFM micrographs confirmed the experimental results and proved that the surface roughness increased upon an increase in plasma power.
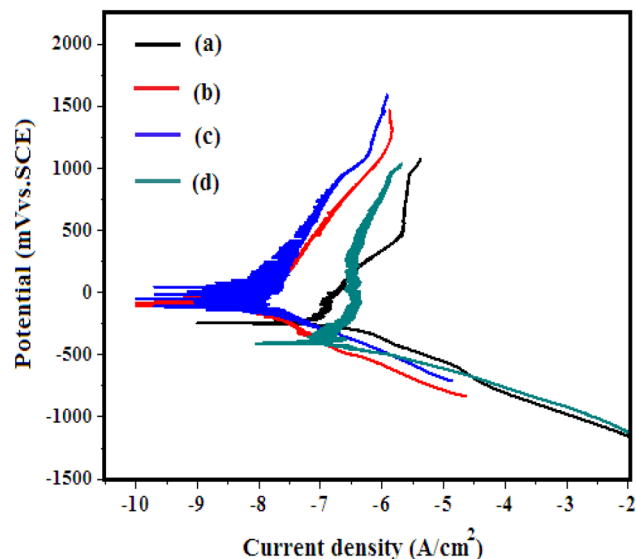

Fig. 9 Polarization curves of the (a) stainless steel substrate and samples grown at various plasma power: (b) 80 W, (c) 90 W and (d) 100 W
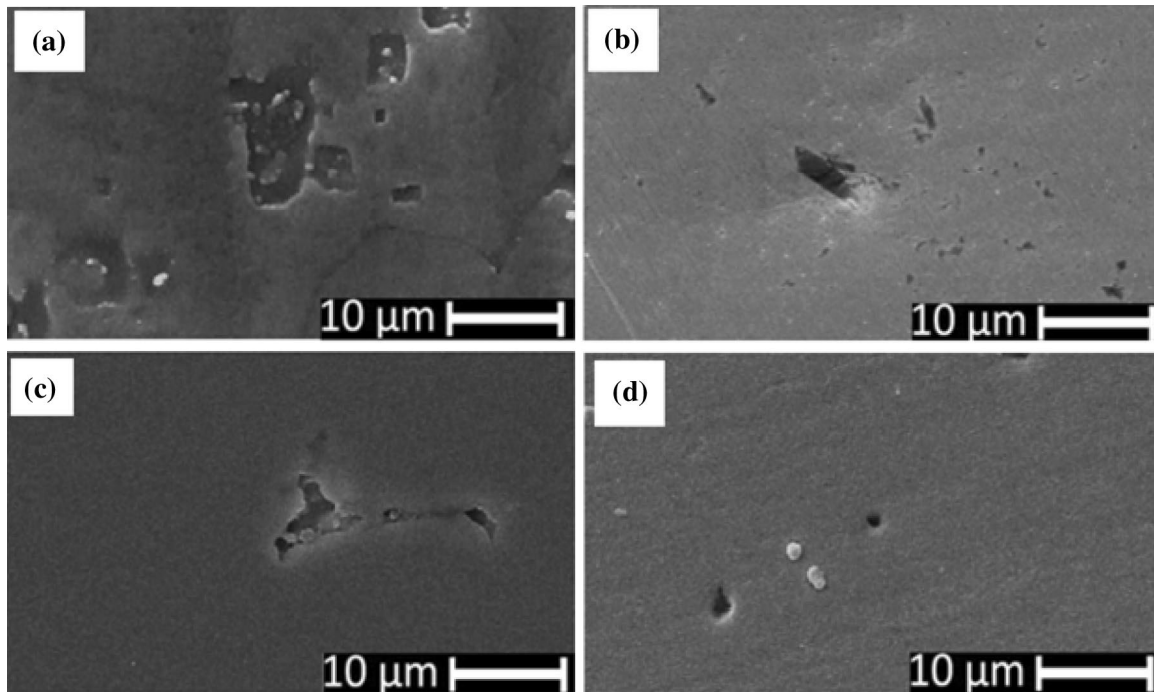
Fig. 10 SEM images after corrosion test of **a** stainless steel substrate and samples grown at various plasma power: **b** 80 W, **c** 90 W, and **d** 100 W

Appendix

The statistical parameters of 3D surface roughness, according with ISO 25178-2:2012 [2] and ASME B46.1-2009 [3], are defined as follows:

Amplitude parameters

The amplitude properties are described by six parameters, which give information about the statistical average properties, the shape of the height distribution histogram, and about extreme properties.

(Sa): Arithmetical mean height is the mean surface roughness.

(Sq): Root mean square height is the standard deviation of the height distribution, or RMS surface roughness.

(Ssk): Skewness is the third statistical moment, quantifying the symmetry of the height distribution. Negative skew indicates a predominance of valleys, while positive skew is seen on surfaces with peaks.

(Sku): Kurtosis is the fourth statistical moment, quantifying the flatness of the height distribution. For spiky surfaces, Sku > 3; for bumpy surfaces, Sku < 3; perfectly random surfaces have kurtosis of 3. (Sp): Maximum peak height is the height between the highest peak and the mean plane.

(Sz): Maximum height is the height between the highest peak and the deepest valley.

(S10z): Ten point height is the average height of the five highest local maximums plus the average height of the five lowest local minimums.

(Sv): Maximum valley depth is the largest valley depth value.

(Sp): Maximum peak height is the largest peak height value.

Hybrid parameters

The hybrid parameters are described by three parameters. These parameters reflect slope gradients and their calculations are based on local z-slopes.

(Ssc): Mean summit curvature is the average of the principal curvature of the local maximums on the surface.

(Sdq): Root mean square gradient is the RMS-value of the surface slope within the sampling area.

(Sdq6): Area root mean square slope is similar to the Sdq but includes more neighbor pixels in the calculation of the slope for each pixel.

(Sdr): Surface area ratio expresses the increment of the interfacial surface area relative to the area of the projected (flat) x,y plane.

(S2A): Projected area expresses the area of the flat x,y plane as given in the denominator of R10.

(S3A): Surface area expresses the area of the surface area taking the z height into account as given in the numerator of R10.

Functional parameters

The functional parameters are described by six parameters. The functional parameters are defined from the surface bearing area ratio curve and are used for characterizing bearing and fluid retention properties.

(Sbi): Surface bearing index. For a Gaussian height distribution Sbi approaches 0.608 for increasing number of pixels. Large Sbi indicates a good bearing property.

(Sci): Core fluid retention index. For a Gaussian height distribution Sci approaches 1.56 for increasing number of pixels. Large values of Sci indicate that the void volume in the core zone is large.

(Svi): Valley fluid retention index. For a Gaussian height distribution Svi approaches 0.11 for increasing number of pixels. Large values of Svi indicate large void volumes in the valley zone. For all surfaces Svi is between 0 and 0.2.

(Spk): Reduced summit height is a measure of the peak height above the core roughness.

(Sk): Core roughness depth is a measure of the "core" roughness (peak-to-valley) of the surface with the predominant peaks and valleys removed.

(Svk): Reduced valley depth is a measure of the valley depth below the core roughness.

Spatial parameters

(Sds): Density of summits is the number of local maximums per area.

(Std): Texture direction is defined as the angle of the dominating texture in the image. For images consisting of parallel ridges, the texture direction is parallel to the direction of the ridges. If the ridges are perpendicular to the X-scan direction Std = 0.

(Stdi): Texture direction index is a measure of how dominant the dominating direction is, and is defined as the average amplitude sum divided by the amplitude sum of the dominating direction.

(Srw): Dominant radial wavelength is the dominating wavelength found in the radial spectrum.

(Srwi): Radial wave index is a measure of how dominant the dominating radial wavelength is, and is defined as the average amplitude sum divided by the amplitude sum of the dominating wavelength. Srwi is always between 0 and 1. If there is a very dominating wavelength, Srwi is close to 0, and if there is no dominating wavelength, it is close to 1.

(Shw): Mean half wavelength.

(Scl20): Correlation length at 20% is the horizontal distance of the areal autocorrelation function that has the fastest decay to 20%.

(Scl37): Correlation length at 37% is the horizontal distance of the areal autocorrelation function that has the fastest decay to 37% (37% is equivalent to 1/e). For an anisotropic surface the correlation length is in the direction perpendicular to the surface lay.

(Str20): Texture-aspect ratio at 20% is the ratio of the fastest to slowest decay to correlation 20% of the autocorrelation function. In principle, the texture-aspect ratio has a value between 0 and 1. For a surface with a dominant lay, the parameters will tend towards 0, whereas a spatially isotropic texture will result in a Str value of 1.

(Str37): Texture-aspect ratio at 37% is the ratio of the fastest to slowest decay to correlation 37% of the autocorrelation function.

(Sch): Cross hatch angle is the angle difference between the two most dominant angles found in the image by analyzing its autocorrelation function.

- The Area Power Spectral Density function (APSD) for an image z(x,y) is defined [ASME B46.1-2009] as the square of the amplitude of the Fourier transform of the image normalized by the area size of a pixel.

References

1. D. Dastan, S.W. Gosavi, N.B. Chaure, Studies on electrical properties of hybrid polymeric gate dielectric for field effect transistors. Macromol. Symp. **347**, 81–86 (2015)
2. Z. Shi, J. Wang, F. Mao, C. Yang, C. Zhang, R. Fan, Significantly improved dielectric performances of sandwich-structured polymer composites induced by alternating positive-k and negative-*k* layers. J. Mater. Chem. A **5**(28), 14575–14582 (2017)
3. X. Zhu, J. Yang, D. Dastan, H. Garmestani, R. Fan, Zh Shi, Fabrication of core-shell structured Ni@BaTiO3 scaffolds for polymer composites with ultrahigh dielectric constant and low loss. Composites A **125**, 105521 (2019)
4. S.L. Panahi, D. Dastan, N.B. Chaure, Characterization of zirconia nanoparticles grown by sol-gel method. Adv. Sci. Lett. **22**, 941–944 (2016)
5. J. Wang, Z. Shi, F. Mao, S. Chen, X. Wang, Bilayer polymer metacomposites containing negative permittivity layer for new high-k materials. ACS Appl. Mater. Interfaces **9**(2), 1793–1800 (2017)
6. S. Abbasi, M. Hasanpour, F. Ahmadpoor, M. Sillanpää, D. Dastan, A. Achour, Application of the statistical analysis methodology for photodegradation of methyl orange using a new nanocomposite contining modified TiO_2 semiconductor with SnO_2. Int. J. Environ. Anal. Chem. (2019). https://doi.org/10.1080/03067319.2019.1662414
7. L. Aljerf, D. Dastan, S. Sajjadifar, S. Bhatnagar, P.O. Ukaogo, F. Dehmchi, Guidelines for the preparation and isolation of Radionuclides produced with in-house cyclotrons bombardments. Open J. Chem. **5**(1), 020–029 (2019)
8. C. Zhang, Z.C. Shi, F. Mao, C. Yang, X. Zhu, J. Yang, H. Zuo, R. Fan, Flexible polyimide nanocomposites with DC bias induced excellent dielectric tunability and unique non-percolative negative-k towards intrinsic metamaterials. ACS Appl. Mater. Interfaces **10**(31), 26713–26722 (2018)
9. X.-T. Yin, D. Dastan, F.-Y. Wu, J. Li, Facile synthesis of SnO_2/$LaFeO_3 - XNX$ composite: photocatalytic activity and gas sensing performance. Nanomaterials **9**, 1163 (2019)
10. D. Dastan, Nanostructured anatase titania thin films prepared by sol-gel dip coating technique. J. At. Mol. Condens. Nano Phys. **2**, 109–114 (2015)

11. J. Zhao, M. Konh, A. Teplyakov, Surface chemistry of thermal dry etching of cobalt thin films using hexafluoro acetyl acetone (hfacH). Appl. Surf. Sci. **455**, 438–445 (2018)

12. J.M. Rodrigues, M. Filipa Ribeiro, E.C. Fernandes, Catalytic activity of electrodeposited cobalt oxide films for methane combustion in a micro-channel reactor. Fuel **232**, 51–59 (2018)

13. M. Manickam, V. Ponnuswamy, C. Sankar, R. Suresh, Cobalt oxide thin films prepared by NSP technique: impact of molar concentration on the structural, optical, morphological and electrical properties. Optik **127**, 5278–5284 (2016)

14. X.-T. Yin, W.-D. Zhou, J. Li, Q. Wang, F.-Y. Wu, D. Dastan, D. Wang, H. Garmestani, X.-M. Wang, S. Talu, A highly sensitivity and selectivity Pt-SnO$_2$ nanoparticles for sensing applications at extremely low level hydrogen gas detection. J. Alloys Compd. **805**, 229–236 (2019)

15. C.W. Kung, C.Y. Lin, R. Vittal, K.C. Ho, Synthesis of cobalt oxide thin films in the presence of various anions and their application for the detection of acetaminophen. Sens. Actuators B **182**, 429–438 (2013)

16. X.-T. Yin, W.-D. Zhou, J. Li, P. Lv, Q. Wang, D. Wang, F.-Y. Wu, D. Dastan, H. Garmestani, Zh Shi, Ş. Tălu, Tin dioxide nanoparticles with high sensitivity and selectivity for gas sensors at sub-ppm level of hydrogen gas detection. J. Mater. Sci.: Mater. Electron. **30**, 14687–14694 (2019)

17. T. Maruyama, T. Nakai, Cobalt thin films prepared by chemical vapor deposition from cobaltous acetate. Appl. Phys. Lett. **59**, 1433–1434 (1991)

18. M.E. Dondersa, H.C.M. Knoopsa, M.C.M. Van, Remote plasma atomic layer deposition of Co$_3$O$_4$ thin films. J. Electrochem. Soc. **158**, 111–120 (2011)

19. D. Dastan, B. Nandu, Chaure influence of surfactants on TiO$_2$ nanoparticles grown by sol-gel technique. J. Mater. Mech. Manufact. **2**, 21–24 (2014)

20. B. Han Kyu, H. Choia, K. Parka, Low-temperature atomic layer deposition of cobalt oxide thin films using dicobalt hexacarbonyl tert-buty lacetylene and ozone. Electrochem. Solid State Lett. **15**, 58–62 (2011)

21. T. Maruyama, S. Arai, Cobalt oxide thin films prepared by chemical vapor deposition from cobalt (II) acetate. J. Electrochem. Soc. **143**, 1383–1386 (1996)

22. D. Dastan, U. Priyanka, B. Londhe, N. Chaure, Characterization of TiO$_2$ nanoparticles prepared using different surfactants by sol–gel method. J. Mater. Sci.: Mater. Electron. **25**, 3473–3479 (2014)

23. S. Junga, D.K. Nandia, S. Yeo, Phase-controlled growth of cobalt oxide thin films by atomic layer deposition. Surf. Coat. Technol. **337**, 404–410 (2018)

24. A. Jafari, V. Fayaz, S. Meshkani, S.A.A. Terohid, Interaction between plasma and tungsten carbide thin films coated on stainless steel as tokamak reactor first wall. Philipp. J. Sci. **147**, 537–543 (2018)

25. Chisung Ahn et al., Low-temperature synthesis of large-scale molybdenum disulfide thin films directly on a plastic substrate using plasma-enhanced chemical vapor deposition. Adv. Mater. **27**(35), 5223–5229 (2015)

26. A.M. Nardes, A.M. de Andrade, F.J. Fonseca, E.A.T. Dirani, R. Muccillo, E.N.S. Muccillo, Low-temperature PECVD deposition of highly conductive microcrystalline silicon thin films. J. Mater. Sci.: Mater. Electron. **14**, 407–411 (2003)

27. I.-S. Lee, J.-W. Kim, C.-J. Youn, S.-K. Park, Y.-B. Hahn, Preparation and characterization of TiO$_2$ thin films by PECVD on Si substrate. Korean J. Chem. Eng. **13**, 473–477 (1996)

28. D. Zhao, D.A. Mourey, T.N. Jackson, Low-temperature pulsed-PECVD ZnO thin-film transistors. J. Electron. Mater. **39**, 554–558 (2010)

29. L. Liu, Y.Y. Sheng, M. Liu, M. Dienwiebel, Zh Zhang, D. Dastan, Formation mechanism of tribo-layers for brass during sliding test under lubricated condition. Tribol. Int. **140**, 105727 (2019)

30. A. Jafari, M. Ghoranneviss, M.R. Hantehzadeh, A. Boochani, Effect of plasma power on growth of multilayer graphene on copper using plasma enhanced chemical vapour deposition. J. Chem. Res. **40**, 40–43 (2016)

31. Chemical Vapour Deposition. Precursors, Processes and Applications. Edited by Anthony C. Jones and Michael L. Hitchman. Royal Society of Chemistry, Cambridge 2008

32. Carbide, Nitride and Boride Materials Synthesis and Processing, Plasma-Enhanced Chemical Vapor Deposition (PECVD), Stevenx R. Droes Toivo T. Kodas, Mark J. Hampden-Smith, pp 579-603

33. G. Cao, Y. Wang, *Nanostructures and Nanomaterials Synthesis, Properties and Applications* (World Scientific Publishing, Singapore, 2011), p. 248

34. D. Dastan, Effect of preparation methods on the properties of titania nanoparticles: solvothermal versus sol-gel. Appl. Phys. A **123**, 1–13 (2017)

35. A. Meidanchi, A. Jafari, Synthesis and characterization of high purity Ta$_2$O$_5$ nanoparticles by laser ablation and its antibacterial properties. Opt. Laser Technol. **111**, 89–94 (2019)

36. D. Dastan, N. Chaure, M. Kartha, Surfactants assisted solvothermal derived titania nanoparticles: synthesis and simulation. J. Mater. Sci.: Mater. Electron. **28**, 7784–7796 (2017)

37. S.A.A. Terohid, S. Heidari, A. Jafari, S. Asgary, Effect of growth time on structural, morphological and electrical properties of tungsten oxide nanowire. Appl. Phys. A **124**, 567–576 (2018)

38. D. Dastan, L.S. Panahi, N.B. Chaure, Characterization of titania thin films grown by dip-coating technique. J. Mater. Sci.: Mater. Electron. **27**, 12291–12296 (2016)

39. A. Jafari, M. Mosavat, A. Meidanchi, H. Hossienkhani, Growth of boron carbide nanostructures on silicon using hot filament chemical vapour deposition. J. Chem. Res. **42**, 73–76 (2018)

40. F.M. El-Hossary, A.M. Abd El-Rahman, M. Raaif, S. Qu, J. Zhao, M.F. Maitz, M. Abo El-Kassem, Effect of DC-pulsed magnetron sputtering power on structural, tribological and biocompatibility of Ti–Zr–N thin film. Appl. Phys. A **124**, 42 (2018)

41. M.J. Thwaites, S. Rand, P.J. Grundy, K. O'Grady, Novel sputtering technology for grain-size control marian vopsaroiu. IEEE Trans. Magn. **40**, 4 (2004)

42. M.R. Amirzada, A. Tatzel, V. Viereck, H. Hillmer, Surface roughness analysis of SiO$_2$ for PECVD, PVD and IBD on different substrates. Appl. Nanosci. **6**, 215–222 (2016)

43. É.C. Oliveira, S.A. Cruz, P.H.L. Aguiar, Effect of PECVD deposition parameters on the DLC/PLC composition of a-C: H thin films. J. Braz. Chem. Soc. **23**, 1657–1662 (2012)

44. G. Korotchenkov, *Thin Metal Films. Handbook of Gas Sensor Materials. Integrated Analytical Systems* (Springer, New York, 2013), pp. 153–166

45. F. Family, T. Vicsek, Dynamics of Fractal Surfaces (World Scientific, Singapore, 1991); A-L. Barab´asi and H. E. Stanley, Fractal Concepts in Surface Growth (Cambridge Press, Cambridge, 1995)

46. S. Pal, D.P. Landau, The Edwards–Wilkinson model revisited: large-scale simulations of dynamic scaling in 2 + 1 dimensions Physica A: Statistical Mechanics and its Applications, 267, (1999) 406-413

47. SPIPTM 6.7.7 software (Copyright © 1998-2018 Image Metrology A/S). http://www.imagemet.com. Accessed 1 Mar 2019)

48. ISO 25178-2: 2012, Geometrical product specifications (GPS) - Surface texture: Areal - Part 2: Terms, definitions and surface texture parameters. http://www.iso.org. Accessed 1 Mar 2019

49. American Society of Mechanical Engineers (2009), ASME B46.1-2009, Surface Texture (Surface Roughness, Waviness and Lay),

ASME. New York, NY, USA. https://www.asme.org. Accessed 1 Mar 2019

50. Ş. Ţălu, *Micro and Nanoscale Characterization of Three Dimensional Surfaces. Basics and Applications* (Napoca Star Publishing House, Cluj-Napoca, 2015)

51. D. Dudeck et al., First nucleation steps during deposition of SiO_2 thin films by plasma enhanced chemical vapour deposition. Surf. Sci. **601**(10), 2223–2231 (2007)

52. S.H. Lee, M.G. So, Effects of deposition temperature and pressure of the surface roughness and the grain size of polycrystalline Si1xGex lms. J. Mater. Sci. **35**(19), 4789–4794 (2000)

53. M. Ohring, *Material science of thin films, deposition and structures*, 2nd edn. (Academic Press, San Diego, 2002)

54. M. Bahaa, A. Zied, A novel foam combustion approach for the synthesis of nano-crystalline cobalt oxide powder. Ceram. Int. **45**, 4540–4548 (2019)

55. U.D. Wdowik, K. Parlinski, Phys. Rev. B **75**, 104306/1–104306/6 (2007)

56. S. Sindhu, M. Heiler, K.M. Schindler, W. Widdra, H. Neddermeyer, Surf. Sci. **566**(567), 471–475 (2004)

57. Z.X. Shen, J.W. Allen, P.A.P. Lindberg, D.S. Dessau, B.O. Wells, A. Borg, W. Ellis, J.S. Kang, S.J. Oh, I. Lindau, W.E. Spicer, Phys. Rev. B **42**, 1817–1828 (1990)

58. D. Dastan, A.G. Banpurkar, Solution processable sol-gel derived titania gate dielectric for organic field effect transistors. J. Mater. Sci.: Mater. Electron. **28**(4), 3851–3859 (2016)

59. S. Al-Saadi, R.K. Singh Raman, A long aliphatic chain functional silane for corrosion and microbial corrosion resistance of steel. Prog. Org. Coat. **127**, 27–36 (2019)

60. D. Dastan, S.L. Panahi, A.P. Yengantiwar, A.G. Banpurkar, Morphological and electrical studies of titania powder and films grown by aqueous solution method. Adv. Sci. Lett. **22**, 950–953 (2016)

61. S.K. Ghosh, G.K. Dey, R.O. Dusane, A.K. Grover, Improved pitting corrosion behaviour of electrodeposited nanocrystalline Ni-Cu alloys in 3.0 wt% NaCl solution. J. Alloys Compd. **426**, 235–243 (2006)

62. S.H. Mosavat, M.H. Shariat, M.E. Bahrololoom, Study of corrosion performance of electrodeposited nanocrystalline Zn-Ni alloy coatings. Corros. Sci. **59**, 81–87 (2012)

63. A. Aledresse, A. Alfantazi, A study on the corrosion behavior of nanostructured electrodeposited cobalt. J. Mater. Sci. **39**, 1523–1526 (2004)

64. F.R. Morral, Corrosion of cobalt and cobalt alloys. Corrosion **25**(7), 307–322 (1969)

65. C.S. Brandolt, M.R. Ortega Vega, T.L. Menezes, R.M. Schroeder, C.F. Malfatti, Corrosion behavior of nickel and cobalt coatings obtained by high-velocity oxy-fuel (HVOF) thermal spraying on API 5CT P110 steel. Mater. Corros. **4**, 67 (2016)